Combustion and Flame 161 (2014) 347–362

Contents lists available at ScienceDirect

Combustion and Flame

journal homepage: www.elsevier.com/locate/combustflame

Modeling of ammonium dinitramide (ADN) monopropellant combustion with coupled condensed and gas phase kinetics

Piyush Thakre *, Yi Duan, Vigor Yang

School of Aerospace Engineering, Georgia Institute of Technology, Atlanta, GA 30332-0150, USA

ARTICLE INFO

Article history:
Received 28 May 2013
Received in revised form 12 August 2013
Accepted 12 August 2013
Available online 24 September 2013

Keywords:
Ammonium dinitramide
ADN propellant combustion

ABSTRACT

A comprehensive multi-phase combustion model has been developed to study the physiochemical processes involved in the combustion of ammonium dinitramide (ADN). The numerical model is based on the conservation equations of mass, species concentration, and energy, and takes into account finite-rate chemical kinetics in both condensed and gas phases. Based on an extensive review of the literature on ADN thermal decomposition, three global decomposition reactions in the condensed phase of ADN are included. A detailed chemical kinetics scheme involving 34 species and 165 reactions is employed in the gas phase. Detailed combustion-wave structures and burning rate characteristics of ADN are described. The optimized gas-phase kinetics mechanism was able to predict the multi-stage flame structure. Good agreements between the predicted and measured profiles of temperature and species mole fractions were obtained at different pressures. Reasonable agreements between calculated and measured values of propellant burning rates and surface temperatures were obtained over a broad range of pressure from 0.7 to 350 atm. The burning rate increases with pressure, except in the mid range of ~60–100 atm. The coupled condensed- and gas-phase analysis employed in the current model is able to capture this irregular/unstable combustion behavior in the mid range, where the burning rate decreases with the increase in pressure.

1. Introduction

Ammonium dinitramide (ADN) is a novel energetic material that can be used as a liquid monopropellant or as an ingredient in solid-rocket propellants [1]. It is a low-signature environmentally friendly propellant, with chlorine-free combustion products. Because it offers higher performance than conventional oxidizers, ADN is a promising alternative to Ammonium Perchlorate (AP) and Ammonium Nitrate (AN) [1].

ADN, which is an ionic compound ($NH_4^+[N(NO_2)_2]^-$), was first synthesized in 1971 at the Zelinsky Institute of Organic Chemistry in the former Soviet Union [2–4]. In 1989, it was independently synthesized by the Stanford Research Institute [5,6]. Over the past four decades, significant research has been conducted to study the combustion wave structure and burning-rate characteristics of ADN. Extensive experimental diagnostics [7–13] and theoretical modeling [14–21] have been reported over a broad range of operating conditions. The experimental techniques include T-jump/FTIR spectroscopy [22], micro-thermocouple [9,23,24], UV-spectrophotometry [23,24], molecular beam mass-spectrometry (MBMS) [12,25], differential scanning calorimetry (DSC) [13,26], thermal gravimetry combined with mass spectrometry (TG-MS) [13,26], optical polarizing light microscopy, laser-Raman spectroscopy, and energy dispersive X-ray diffraction techniques [27]. The theoretical methods include *ab initio* calculation based on quantum chemistry [14–16] and numerical models based on detailed chemistry [17–21]. Both self-sustained [22–27] and laser-induced combustion [28,29] have been modeled. A review of the literature on ADN thermal decomposition and its combustion behavior up to 2005 is detailed by Yang et al. [30].

Russell et al. [27] confirmed a reversible phase transition of an ADN crystal, as described by reaction

$$\alpha\text{-ADN} \overset{2.0\ \text{GPa}}{\Longleftrightarrow} \beta\text{-ADN} \qquad (R1)$$

The β-ADN has a new monoclinic polymorphic structure. The melting point of α-ADN is 365–368 K [12,25], significantly lower than RDX (478 K) [31], HMX (551 K) [32], and AP (865 K) [33]. The ADN propellant modeled in the present paper is assumed to be α-ADN, without any curing agent.

Figure 1 shows schematically the physiochemical processes involved in ADN monopropellant combustion. The temperatures mentioned in Fig. 1 are representative of a flame at 5 atm. In order to simplify analysis, the entire combustion wave is segmented into

* Corresponding author. Current address: CD-adapco, Ltd., Melville, NY 11747, USA.

E-mail addresses: piyush.thakre@gmail.com (P. Thakre), vigor@gatech.edu (V. Yang).

0010-2180/$ - see front matter © 2013 The Combustion Institute. Published by Elsevier Inc. All rights reserved.
http://dx.doi.org/10.1016/j.combustflame.2013.08.006

Nomenclature

A	cross-sectional area of propellant sample
A_g	fractional cross-sectional area consisting of gas bubbles in two-phase region
A_j	pre-exponential factor of rate constant of reaction j
A_s	interface area between bubbles and liquid per unit volume
a	pre-exponential factor of burning-rate law
B_j	temperature exponent in rate constant of reaction j
C_i	molar concentration of species i
C_{pi}	constant-pressure specific heat of species i
E_j	activation energy of reaction j
e	internal energy
H_v	enthalpy of vaporization
h	enthalpy
h_i	static enthalpy of species i
h_{fi}°	heat of formation of species i under standard condition
k_j	rate constant of reaction j
$\dot{m}''$	mass flux
N	total number of species
n	pressure exponent
N_R	total number of reactions
p	pressure
p_0	pre-exponential factor of vapor pressure in Arrhenius form
r_b	propellant burning rate
R_u	universal gas constant
T	temperature
T_{melt}	melting point of ADN
T_d	initial decomposition temperature
T_s	temperature at propellant surface
T_a	temperature in aerosol zone
s	sticking coefficient
t	time
u	bulk velocity
V_i	diffusion velocity of species i
D_i	effective mass-diffusion coefficient for species i
D_{Ti}	thermal diffusion ratio
$\bar{v}_n$	average normal velocity component of vapor molecule
W_i	molecular weight of species i
$\dot{w}_i$	mass production rate of species i
$\dot{w}_{Rj}$	mass production rate of reaction j
X_i	molar fraction of species i
Y_i	mass fraction of species i

Greek symbols

ϕ	void fraction
ρ	density
λ	thermal conductivity
$\dot{\omega}$	molar production rate

Subscripts

0^+	gas-phase side of propellant surface
0^-	foam layer side of propellant surface
c	condensed phase
c–g	from condensed phase to gas phase
cond	condensation
eq	equilibrium condition
evap	evaporation
f	mass-averaged quantity in foam layer
g	gas phase
l	liquid phase
s	propellant surface or solid phase
v	vapor

three regions: solid phase, foam layer, and gas phase. For RDX and HMX, the chemical reactions in the solid phase can be ignored, due to the high liquefaction temperature [34]. For ADN, however, the situation is more complicated, as it undergoes significant exothermic reactions in the solid phase. Sharp exothermicity occurred instantly when the first gas product was detected [33]. Brill et al. [22] proposed two sets of initial decomposition pathways, according to observed products ratios and the heat-release. It is suggested that Reaction (R2), which is mildly endothermic, dominates at lower temperatures when the decomposition rate is low.

$$ADN_{(s)} \rightarrow NH_3 + HNO_3 + N_2O \quad (R2)$$

Reaction (R3), which is quite endothermic, is likely to dominate under rapid thermolysis conditions.

$$ADN_{(s)} \rightarrow NH_3 + HN(NO_2)_2 \quad (R3)$$

The product $HN(NO_2)_2$, usually abbreviated as HDN, is not stable and will decompose rapidly through reaction

$$HN(NO_2)_2 \rightarrow NO_2 + HNNO_2 \quad (R4)$$

The gaseous decomposition products form bubbles within the solid ADN. In order to accurately predict ADN combustion characteristics, the solid ADN has been subdivided into two segments, a pure solid ADN layer and a solid-bubble layer (Fig. 1). Assuming that the pure solid ADN layer remains thermally stable, any thermal decomposition can be neglected [35]. Only heat conduction is taken into account in this region. The solid-bubble layer starts around 333 K [30]. ADN thermal decomposition, sublimation, and the gas-phase reactions within bubbles make the physiochemical processes in the solid-bubble layer very challenging to simulate.

When the temperature reaches the melting point of ADN, thermodynamic phase transition occurs as described by R5.

$$ADN_{solid} \rightarrow ADN_{liquid} \quad (R5)$$

The liquid-bubble layer (Fig. 1) starts at about 366 K, close to the melting point of ADN. The thermal decomposition and evaporation of ADN, bubble formation, gas-phase reactions within bubbles, and interfacial transport of mass and energy between the gas and condensed phase also take place in the liquid-bubble layer. In the current approach, since the physiochemical processes in the solid-bubble and liquid-bubble layers are similar, these two layers are treated together as a foam layer (also referred to as the subsurface multi-phase region).

The propellant undergoes a sequence of rapid evaporation and decomposition in the near field immediately above the foam layer. Subsequent degradation and recombination reactions occur among the primary products. These reactions lead to final products and a corresponding flame region. Reaction R6, R7, and R8 are some of the possible chemical pathways in the gas-phase region [30],

$$4NH_3 + 4NO_2 \rightarrow 3N_2 + 2NO + 6H_2O \quad (R6)$$

$$2NH_3 + 2NO_2 \rightarrow NH_4NO_{3(s)} + N_2 + H_2O \quad (R7)$$

$$2NH_3 + 2NO_2 \rightarrow N_2O + N_2 + 3H_2O \quad (R8)$$

A global reaction for ADN condensed-phase thermal decomposition is obtained from the summation of all proposed reactions. Reaction (R9) is also consistent with the measured final composition [17].

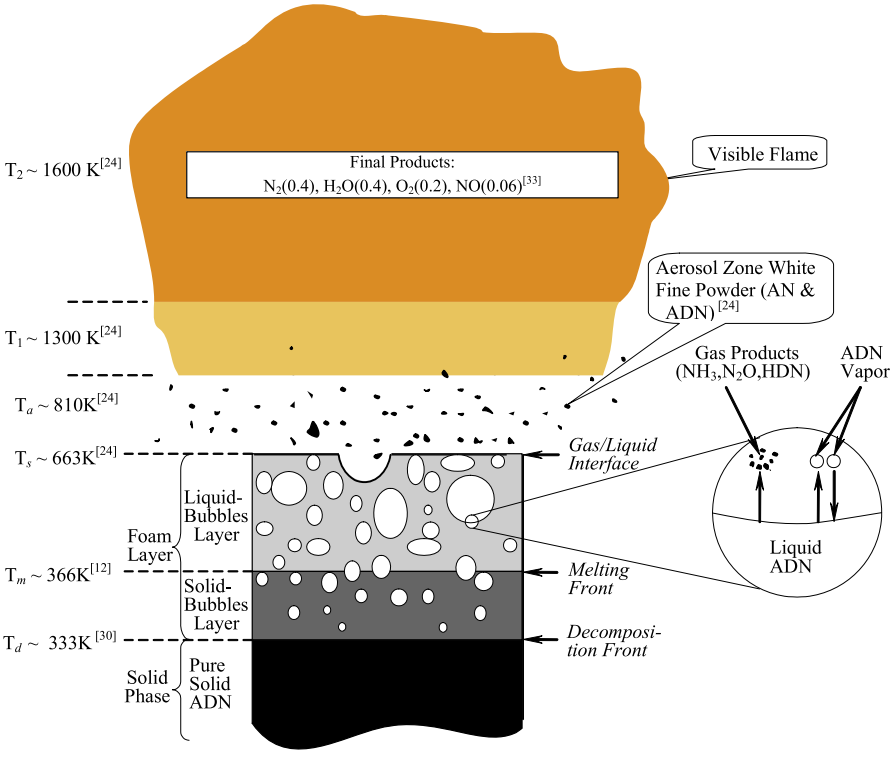

Fig. 1. Schematic of combustion-wave structure of ADN monopropellant (not to scale).

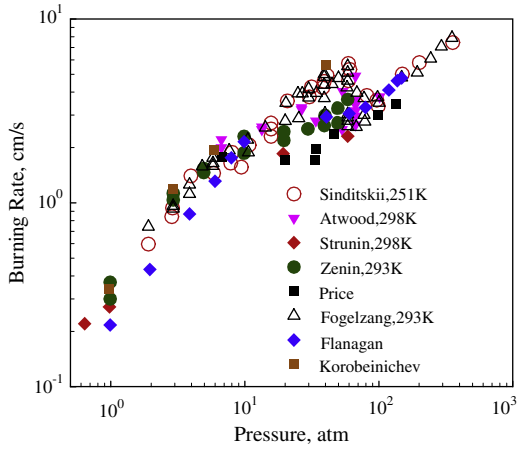

Fig. 2. ADN burning rate vs. pressure from various measurements.

$$12\mathrm{ADN} \rightarrow 3\mathrm{NH_3} + 10\mathrm{N_2O} + 6\mathrm{NO_2} + 15\mathrm{H_2O} + 2\mathrm{NO} + 6\mathrm{N_2} + \mathrm{HNO_3} + 2\mathrm{NH_4NO_{3(s)}} \quad \text{(R9)}$$

ADN has a higher burning rate than AP, RDX, and HMX. At 5 atm, the ADN burning rate of 15 mm/s [9] is about ~10 times higher than those of HMX (1.2 mm/s) [36] and RDX (1.5 mm/s) [37]. ADN exhibits a unique burning-rate irregularity in the pressure range of 40–100 atm, as confirmed by many researchers [4,9–11,23,24,27,38,39]. The burning-rate in this pressure range not only has a lot of scatter, but also appears to decrease slightly with increasing pressure as shown in Fig. 2 [4,9–11,23,24,27,38,39].

Two stable combustion regions of ADN exist at pressures below 20 atm and above 100 atm. According to Sinditskii et al. [23,24], the condensed-phase decomposition appears to dominate in the low-pressure region. Below 20 atm, a significant amount of heat release from the condensed phase ADN decomposition sustains the combustion process. The heat feedback from the gas phase can be ignored, on account of a low temperature gradient at the propellant burning surface [9,24]. They also speculate that the condensed-phase species (ADN and AN) are dispersed into the gas flame due to the high burning rate. The white aerosol zone [24] and condensed material dispersion in other condensed-phase dominating type of combustion [40] seem to support their assumption. According to Sinditskii et al. [23,24], as the pressure increases more energy is required for ADN dissociation. The condensed-phase heat release, however, stays nearly constant, while the gas-phase heat feedback is still insignificant. In this mid-pressure range, there appears to be a gap between the energy required to heat up and evaporate the condensed-phase materials and the heat released in the condensed phase; this leads to oscillating and unstable combustion behavior and causes the observed burning-rate data scatter. The competition between the fast but energy-limited heat-release process in the condensed phase and the slow but energy-rich heat-release process in the gas phase is considered to be responsible for the burning-rate irregularity in the 40–100 atm pressure range. At higher pressures, the gas-phase flame is much closer to the burning surface, resulting in a steep temperature gradient and heat feedback to the condensed phase; the gas-phase heat feedback is adequate to sustain ADN deflagration.

In order to analyze the ADN combustion wave and its burning characteristics, many computational studies have been performed based on detailed chemical reactions by many researchers [14–21]. One of the first detailed gas-phase kinetics mechanisms was developed by Ermolin in 1990s [19] and improved in 2004 [30]. A mechanism with 32 species and 152 reactions was proposed by Lin and Park based on their *ab initio* MO/**c**VRRKM calculations [16]. Incorporating Park's scheme and several H/N/O reactions, which have been well developed for RDX combustion [35], a more comprehensive ADN gas-phase combustion kinetics mechanism was employed by Liau et al. [17]. The analysis of ADN self-deflagration at 6 atm obtained a good agreement between predicted and

measured results. Based on a sub-mechanism (22 species and 98 reaction) for nitramine propellant combustion suggested by Yetter et al. [41] and 74 additional reactions for ADN decomposition products proposed by Park et al. [16], Korobeinichev et al. [42] developed a 33 species and 172 reaction kinetics mechanism. A kinetics mechanism including more than 100 reactions was used by Shmakov et al. to model thermal decomposition of ADN vapor in a two-temperature flow reactor [43].

None of the ADN combustion models mentioned above link the condensed- and gas-phase kinetics, due to the lack of reliable decomposition mechanism and data on the properties of ADN liquid and its intermediate products. The experimental data available at the surface or in the gas phase were used as initial conditions in those detailed gas-phase combustion models. In order to circumvent the limitations of the previous combustion models, an improved model that couples the condensed and gas-phase kinetic mechanism is needed. Such a model should also be able to capture the irregularity of ADN burning in the mid-pressure range.

The first model to couple a global condensed-phase reaction with detailed gas-phase kinetics was developed by Gross et al. [21,33] Reasonably good agreement of predicted and measured burning rate in the low pressure (3–10 atm) and high pressure (100–200 atm) ranges was obtained. A proposed modification of the interpretation of erratic combustion behavior in the pressure range of 10–100 atm offered by Sinditskii et al. [23,24] was presented. Table 1 summarizes the ADN combustion models of several researchers.

2. Theoretical formulation

To facilitate analysis, the coordinate system is fixed at the ADN propellant burning surface. A quasi one-dimensional model is formulated as a first approximation of the problem. A brief summary of the theoretical formulation of the physiochemical processes in various regions is described in the following sections.

2.1. Solid phase region

Thermal decomposition of ADN and radiation absorption is ignored in modeling the solid-phase process. Only heat conduction governed by the following equation is considered:

$$\rho_s c_{p,s}\frac{\partial T_s}{\partial t}+\rho_s u_s c_{p,s}\frac{\partial T_c}{\partial x}=\frac{\partial}{\partial x}\left(\lambda_s\frac{\partial T_s}{\partial x}\right) \tag{1}$$

A closed-form solution of Eq. (1) at steady state is available, subject to appropriate boundary conditions and the propellant burning rate.

The various properties employed in the present work are summarized in Table 2. The thermal conductivity and specific-heat capacity of solid ADN are available in various Refs. [5,8,9,13,29,34,47,48]. The measurement of liquid ADN properties is difficult because decomposition usually takes place before melting, although the density of liquid has been reported by Velardez et al. [49]. Hence, the liquid properties are assumed to be identical to those in the solid phase. Systematic parametric calculations were performed in the current work, due to availability of various thermodynamic data for the condensed phase. The values used in the model appear in bold in Table 2.

Table 2
Thermodynamic and transport properties of ADN.

Parameter	Units	Value	Ref. or Comments
$c_{p,\mathrm{ADN}(s)}$	cal/g/K	$2.094\times10^{-1}+3.361\times10^{-4}T$	[44]
	cal/g/K	0.59	[45]
	J/kg/K	1.26×10^{3}	[46]
	cal/g/K	**0.49**	[24]
$c_{p,\mathrm{ADN}(l)}$			$c_{p,\mathrm{ADN}(l)}=c_{p,\mathrm{ADN}(s)}$
$\lambda_{p,\mathrm{ADN}(s)}$	cal/cm/s/K	$\mathbf{1.238\times10^{-3}-5.78\times10^{-7}}T$	[44]
	cal/cm/s/K	0.00193	[45]
	J/m/s/K	0.419	[46]
$\lambda_{p,\mathrm{ADN}(l)}$			$\lambda_{p,\mathrm{ADN}(l)}=\lambda_{p,ADN(s)}$
$\rho_{p,\mathrm{ADN}(s)}$	g/cm^3	**1.60**–1.84	[46]
$\rho_{p,\mathrm{ADN}(l)}$	g/cm^3	**1.55**	[49]
$H_{v,\mathrm{ADN}}$	kcal/mol	35.1–**37.1**	[43]
$H_{melting,\mathrm{ADN}}$	cal/g	**32**	[9]
	kcal/mol	3.4	[5]

2.2. Foam layer region

The foam layer consists of the solid-bubble and liquid-bubble layers (Fig. 1). The physiochemical processes in this region are extremely complex, involving thermal decomposition, sublimation, evaporation, condensation, bubble formation, gas-phase reactions in bubbles, and interfacial transport of mass and energy between the gas and condensed phases. A two-phase fluid dynamics model based on a spatial averaging technique is employed to formulate these complicated phenomena [35]. The analysis is based on the integral form of the conservation laws for control volumes occupied separately by the bubbles and condensed phases. In establishing the gas-phase formulation, the Dupuit-Forchheimer [47] fractional-volume voidage definition is employed, given by

$$A_g=\phi A \tag{2}$$

With the additional assumption that mass diffusion is negligible, the conservation equations for both condensed phase and gas phase can be combined and written as follows.

Mass

$$\frac{\partial[(1-\phi)\rho_c+\phi\rho_g]}{\partial t}+\frac{\partial}{\partial x}[(1-\phi)\rho_c u_c+\phi\rho_g u_g]=0 \tag{3}$$

Condensed species concentration

$$\frac{\partial[(1-\phi)\rho_c Y_{c_i}]}{\partial t}+\frac{\partial}{\partial x}[(1-\phi)\rho_c u_c Y_{c_i}]=\dot{w}_{c_i}\quad(i=1,2,\ldots,N_c) \tag{4}$$

Gaseous species concentration

$$\frac{\partial(\phi\rho_g Y_{g_i})}{\partial t}+\frac{\partial(\phi\rho_g u_g Y_{g_i})}{\partial x}=\dot{w}_{g_i}\quad(i=1,2,\ldots,N_g) \tag{5}$$

Table 1
Comparison of ADN combustion models.

Authors	Num. of species	Num. of reactions	Characteristics	Ref.
Ermolin (1996)	26	256	Gas phase kinetic, experimental data were employed as boundary conditions.	[19]
Park et al. (1998)	33	152		[16]
Liau et al.(1998)	33	180		[17]
Korobeinichev et al. (2001)	33	172		[42]
Shmakov et al.(2001)		>100		[43]
Ermolin (2004)	34	218		[20]
Gross et al. (2006)	33	173	Coupled condensed and gas phase kinetics	[21]
Present model	34	165	Optimized gas phase kinetics, coupled with condensed phase reactions	

Energy

$$\rho_f c_f \frac{\partial T_f}{\partial t} - \frac{\partial p}{\partial t} + \rho_f u_f c_f \frac{\partial T_f}{\partial x} = \frac{\partial}{\partial x}\left(\lambda_f \frac{\partial T_f}{\partial x}\right) - \sum_{i=1}^{N_g} \dot{w}_{g_i} h_{g_i} - \sum_{i=1}^{N_g} \dot{w}_{c_i} h_{c_i} + \sum_{i=1}^{N_g} h_{g_i} Y_{g_i} \dot{w}_{c-g} - \sum_{i=1}^{N_c} h_{c_i} Y_{c_i} \dot{w}_{c-g} \quad (6)$$

The properties are mass-averaged as follows

$$\rho_f c_f = [(1-\phi)\rho_c c_c + \phi \rho_g c_g] \quad (7)$$

$$\rho_f u_f c_f = [(1-\phi)\rho_c u_c c_c + \phi \rho_g u_g c_g] \quad (8)$$

$$\lambda_f = [(1-\phi)\rho_c u_c \lambda_c + \phi \rho_g u_g \lambda_g]/[(1-\phi)\rho_c u_c + \phi \rho_g u_g] \quad (9)$$

$$c_c = \sum_{i=1}^{N_c} c_{c_i} Y_{c_i} \quad (10a)$$

$$c_g = \sum_{i=1}^{N_g} c_{g_i} Y_{g_i} \quad (10b)$$

$$\lambda_c = \sum_{i=1}^{N_c} \lambda_{c_i} Y_{c_i} \quad (10c)$$

$$\lambda_g = \sum_{i=1}^{N_g} \lambda_{g_i} Y_{g_i} \quad (10d)$$

The mass and energy production terms depend on the specific chemical reaction mechanisms. The model accommodates the thermal decomposition of ADN, as well as subsequent reactions in the foam layer. The formation of gas bubbles due to sublimation, evaporation and thermal degradation is also considered. Two global decomposition reactions (R10 and R11) are employed for ADN decomposition, as listed in Table 3. Reaction (R10) was proposed by Brill et al., based on measured composition at the burning surface [22]. It should be noted that reaction (R10) is identical to reaction (R9). Reaction R10 is highly exothermic, and provides a major heat source in the condensed phase. In Ref. [21], the activation energy of ADN decomposition was artificially increased at the rate of 100 cal/mole per 5 atm increase in pressure. The adjustment was necessary to obtain a smooth transition between the low- and high-pressure regions. In the current model, this adjustment was not necessary. Some of the solid AN particles produced by reaction (R10) disperse into aerosol zone, while the remaining particles decompose through reaction (R11), which is a less exothermic reaction, as compared to reaction (R10).

Thermodynamic phase transition (R12) consisting of both evaporation (sublimation) and condensation of ADN, is considered to provide a complete description of the mass transfer process. The exact extent of ADN evaporation is not known with certainty, but most researchers seem to agree that some evaporation does takes place. To achieve the right balance of the condensed- and gas-phase heat flux at the surface, it appears necessary to allow some endothermic ADN evaporation. There are several sets of available data for ADN vapor pressure correlations. The data employed by Gross et al. [21] is used in the present work.

Based on the chemical mechanism given by reactions (R10)–(R12), the species production terms in Eqs. (4) and (5) are listed in Table 4. The production terms for reactions in Table 4 are defined as

$$\dot{w}_{R10} = (1-\phi)\rho_c Y_{c,1} k_1 \quad (11)$$

$$\dot{w}_{R11} = (1-\phi)\rho_c Y_{c,2} k_2 \quad (12)$$

$$\dot{w}_{R12} = A_s(k_{12f} - k_{12b}) = A_s s \bar{\nu}_n C_{\mathrm{ADN}} \left(\frac{P_{v,eq}}{p} - X_{g,3}\right) \quad (13)$$

$$\text{Where } s = 1, \quad p_{v,eq} = p_0 \exp\left(-\frac{H_v}{R_u T}\right) \quad (14)$$

2.3. Gas phase region

The species evolved from the burning propellant surface into the gas phase include vapor ADN and its decomposition products. The modeling of the gas phase is based on the mass, energy, and species transport for a multi-component chemically reacting system of *N* species, and accommodates finite-rate chemical kinetics and variable thermophysical properties. If body forces, viscous dissipation, and radiation absorption are ignored, the conservation equations for an isobaric flow can be written as follows. It should be noted that only the gas phase was taken into account in the current treatment.

Mass

$$\frac{\partial(\rho A)}{\partial t} + \frac{\partial}{\partial x}(\rho u A) = 0 \quad (15)$$

Species concentration

$$\frac{\partial(\rho A Y_i)}{\partial t} + \frac{\partial[\rho A(u+V_i)Y_i]}{\partial x} = \dot{w}_i \quad (i = 1, 2, \ldots, N) \quad (16)$$

Energy

$$\frac{\partial(\rho A e)}{\partial t} + \frac{\partial(\rho A u h)}{\partial x} = \frac{\partial}{\partial x}\left(\lambda A \frac{\partial T}{\partial x} - \sum_{i=1}^{N} \rho A Y_i V_i h_i\right) \quad (17)$$

Table 4
Description of species formation in foam layer.

i	Species	$\dot{w}_{ci}$ or $\dot{w}_{gi}$
1	$ADN_{(s)}$	$-(\dot{w}_{R10} + \dot{w}_{R12})$
2	$AN_{(s)}$	$\frac{1}{6}\frac{W_2}{W_1}\dot{w}_{R10} - \dot{w}_{R11}$
3	$ADN_{(g)}$	$\dot{w}_{R12}$
4	NH_3	$W_4\left(\frac{1}{4}\frac{\dot{w}_{R10}}{W_1} + \frac{1}{12}\frac{\dot{w}_{R11}}{W_2}\right)$
5	N_2O	$W_5\left(\frac{5}{6}\frac{\dot{w}_{R10}}{W_1} + \frac{5}{24}\frac{\dot{w}_{R11}}{W_2}\right)$
6	$H_2O_{(g)}$	$W_6\left(\frac{5}{4}\frac{\dot{w}_{R10}}{W_1} + \frac{21}{12}\frac{\dot{w}_{R11}}{W_2}\right)$
7	NO	$W_7\left(\frac{1}{6}\frac{\dot{w}_{R10}}{W_1} + \frac{1}{24}\frac{\dot{w}_{R11}}{W_2}\right)$
8	N_2	$W_8\left(\frac{1}{2}\frac{\dot{w}_{R10}}{W_1} + \frac{13}{24}\frac{\dot{w}_{R11}}{W_2}\right)$
9	$HNO_{3(g)}$	$W_9\left(\frac{1}{12}\frac{\dot{w}_{R10}}{W_1} + \frac{1}{4}\frac{\dot{w}_{R11}}{W_2}\right)$
10	NO_2	$W_{10}\left(\frac{1}{2}\frac{\dot{w}_{R10}}{W_1} + \frac{1}{8}\frac{\dot{w}_{R11}}{W_2}\right)$

Table 3
Subsurface chemical reactions and rate parameters.

No.	Reactions	*A*	*E* (kcal/mol)	Ref.
R10	$ADN_{(s)} \rightarrow 0.25NH_3 + (5/6)N_2O + 0.5NO_2 + 1.25H_2O + (1/6)NO + 0.5N_2 + (1/12)HNO_3 + (1/6)AN_{(s)}$	3.5e15 s^{-1}	32	[25]
R11	$AN_{(s)} \rightarrow (1/12)NH_3 + (5/24)N_2O + (1/8)NO_2 + (21/12)H_2O + (1/24)NO + (13/24)N_2 + 0.25HNO_3$	2.5e14 s^{-1}	47.2	[50]
R12	$ADN_{(s)} \Longleftrightarrow ADN_{(g)}$	5.0e17 Pa	40	[21]
		5.1e21 Pa	37	[25]
		2.8e20 Pa	40	[43]
		2.5e23 Pa	40	[17]

The specific enthalpy of a mixture is the mass-weighted sum of the species enthalpy h_i,

$$h = \sum_{i=1}^{N} h_i Y_i \quad \text{and } h_i = \int_{T_{ref}}^{T} c_{p_i} dT + h_{f_i}^{\circ} \tag{18}$$

Consequently, the specific internal energy becomes

$$e = h - \frac{p}{\rho} \tag{19}$$

The mass diffusion velocity V_i consists of contributions from both concentration and temperature gradients,

$$V_i = -D_i \frac{1}{X_i}\frac{\partial X_i}{\partial x} + D_i \frac{D_{T_i}}{X_i}\frac{1}{T}\frac{\partial T}{\partial x} \tag{20}$$

Finally, the equation of state for a multi-component system is derived to close the formulation.

$$p = \rho R_u T \sum_{i=1}^{N} \frac{Y_i}{W_i} \tag{21}$$

For a set of N_R elementary reactions involving N species, the reaction equations can be written in the following general form

$$\sum_{i=1}^{N} \nu'_{ij} M_i \underset{k_{bj}}{\overset{k_{fj}}{\rightleftharpoons}} \sum_{i=1}^{N} \nu''_{ij} M_i, \quad j = 1, 2, \ldots, N_R \tag{22}$$

where ν'_{ij} and ν''_{ij} are the stoichiometric coefficients for species i appearing as a reactant in the jth forward and backward reactions, respectively, and M_i is the chemical symbol for species i. The reaction rate constant k_j (either k_{fj} or k_{bj}) is given empirically by the Arrhenius expression

$$k_j = A_j T^{B_j} \exp(-E_j / R_u T) \tag{23}$$

The rate of change of molar concentration of species i by reaction j is

$$\dot{C}_{ij} = (\nu'_{ij} - \nu''_{ij}) \left(k_{fj} \prod_{i=1}^{N} C_i^{\nu'_{ij}} - k_{bj} \prod_{i=1}^{N} C_i^{\nu''_{ij}} \right) \tag{24}$$

The total rate of change of species i in Eq. (16) is obtained by summing up the changes due to all reactions:

$$\dot{w}_i = W_i \sum_{j=1}^{N_R} \dot{C}_{ij} \tag{25}$$

The detailed gas-phase kinetic mechanism employed in the present model was developed by optimizing the mechanism used by Liau et al. [17]. The NO mole fraction in Liau's model was underestimated, and N_2O mole fraction was overestimated. The 13 reactions related to NO consumption and N_2O production were removed. Many parametric variations were performed to get the best agreement between predicted and measured temperature and species concentrations profiles at 3, 6, and 40 atm. Based on this, pre-exponential factors of two reactions ($HNNO_2 + M = OH + N_2O + M$ and $HNNO_2 + NO_2 \Rightarrow HN_3O_4$) were changed slightly. Finally, an optimal 34-species and 165-reaction gas-phase kinetics mechanism was obtained and employed. The chemical kinetics was kept constant for all operating pressures.

2.4. Boundary conditions

There are four boundaries or interfaces in the ADN combustion wave: the far-field boundary of the gas-phase flame, the interface between gas phase and foam layer, the interface between foam layer and solid phase, and the unreacted propellant boundary.

Far-field gas phase boundary

The far-field conditions for the gas phase require that the gradients of flow properties be zero.

$$\frac{\partial \rho}{\partial x} = \frac{\partial u}{\partial x} = \frac{\partial Y_i}{\partial x} = \frac{\partial T}{\partial x} = 0 \quad \text{at } x \to \infty \tag{26}$$

Gas phase and foam layer interface

The physical processes in the gas phase and foam layer must be matched at the propellant burning surface, to provide the boundary conditions for each region. This procedure requires balances of mass and energy, and eventually determines the burning surface conditions and burning rate. With the application of conservation laws to the burning surface, the matching conditions are expressed as follows:

Mass

$$[(1-\phi)\rho_c u_c + \phi \rho_g u_g]_{0^-} = (\rho u)_{0^+} \tag{27}$$

Species concentration

$$[(1-\phi)\rho_c u_c Y_{c_i} + \phi \rho_g u_g Y_{g_i}]_{0^-} = [\rho(u + V_i) Y_i]_{0^+} \tag{28}$$

Energy

$$\left[\lambda_f \frac{dT_f}{dx} + (1-\phi)\rho_c u_c Y_{\mathrm{ADN}_{(c)}} h_{\mathrm{ADN}_{c-g}}\right]_{0^-} = \left(\lambda_g \frac{dT_g}{dx}\right)_{0^+} \tag{29}$$

The temperature is identical on both sides of the interface, but species mass fractions could be different. A distinct phase transition from liquid to vapor ADN is assumed to prevail at the interface [35], giving

$$[(1-\phi)\rho_c u_c Y_{\mathrm{ADN}_{(c)}}]_{0^-} = \left[s \bar{\nu}_n C_{\mathrm{ADN}_{(g)}} \left(\frac{p_{v,eq}}{p} - X_{\mathrm{ADN}_{(g)}} \right) \right]_{0^+} \tag{30}$$

Eqs. (27)–(30), coupled with the assumption that $\rho_l u_l = \rho_g u_g$ and $T_l = T_g$ [48], are sufficient to solve the set of unknowns (u_c, T_s, ϕ, Y_i) at the propellant surface.

Foam layer and solid phase interface

The boundary conditions at the interface between solid phase and foam layer (melting front) are:

$$T_c = T_f = T_d, \quad \text{and } \phi = 0 \text{ at } x = x_d \tag{31}$$

Unreacted propellant boundary (cold boundary)

The boundary condition at the unburned side of the propellant ($x \to -\infty$) is

$$T_s = T_{ini} \quad \text{at } x \to -\infty \tag{32}$$

where T_{ini} is the initial temperature of the propellant.

3. Numerical method

The overall calculation proceeds according to a double-iteration procedure, with propellant surface temperature (T_s) and burning rate (r_b) as the eigenvalues. The inner loop is used to correct T_s and the outer loop to correct r_b. For a given initial guess of T_s and r_b, the conservation equation for the subsurface region is solved first. The resulting species concentrations at the surface are used to determine the boundary conditions for the gas phase through the interfacial matching conditions. The next step involves integration of the gas-phase conservation equations to provide the temperature and species-concentration profiles. The non-equilibrium evaporation represented by Eq. (30) is employed to check the convergence of T_s. If not successful, another inner iteration is performed using an updated value of T_s. The outer iteration follows the same procedure as the inner one, except that r_b is used as the eigenvalue to check the interfacial energy balance given by Eq. (29). Since only the burning rate and surface temperature, but not interfacial species concentrations, are involved in the iterative procedure, the current algorithm performs quite well and significantly reduces the computational burden.

Eqs. (3)–(6) for the foam layer region are solved in an uncoupled manner. The method first estimates the new temperature profile

by solving an inert energy equation. Conservation equations of species concentration and void fraction are then integrated using the fourth-order Runge–Kutta method with the temperature profile. The energy equation is subsequently solved with the newly obtained void fraction and species concentration profiles. Since the conservation equations are solved in an uncoupled fashion, several iterations are required to get a converged solution to satisfy all conservation equations.

Eqs. (15)–(17) for the gas-phase region are also fully coupled. They are solved using the Chemkin-Premix [51] package with some modifications. There are two types of computational difficulties in the present theoretical formulation. One is the stiffness due to a wide variety of time and length scales associated with chemical reactions and transport processes, while the other is the complexity arising from the intertwined matching conditions at the propellant surface. The stiffness problem of the gas-phase processes can be effectively circumvented by using a combined Newton-iteration and time-integration scheme originally developed by Kee et al. [51]. The Newton method functions efficiently for steady-state solutions, but needs a reasonable initial guess for smooth convergence. The time-integration technique is more robust, but less efficient. To optimize the benefits of these two algorithms, calculation usually starts with the Newton method and then switches to the integration scheme when the iteration fails to converge. After another trial solution is obtained with several time-marching steps, the Newton method is resumed to gain efficiency. An adaptive-grid system is employed to further improve the convergence rate, while simultaneously acquiring the spatial resolution of the rapidly varying flow properties in the flame zone.

4. Results and discussion

The results of the current work are divided into two sections. First, the ADN gas-phase kinetics mechanism and flame structure are discussed in detail. Then, results from coupled condensed- and gas-phase analyses are presented to give a complete description of the ADN combustion model.

4.1. Gas-phase combustion analysis

In order to validate the current gas-phase kinetics mechanism, experimental data of Korobeinichev et al. [12,42,52] were employed. The conservation equations in the gas phase are solved and ADN gas-phase flame structures at 3, 6, and 40 atm are computed and analyzed. The boundary conditions for gas species are summarized in Table 5.

Figures 3–5 show a comparison of predicted (lines) and measured (symbols) profiles of temperature and species mole fractions of ADN gas-phase flame at 3 atm. The agreement between predicted and measured temperature profile in Fig. 3 is quite satisfactory. The main products of ADN combustion at 3 atm are H_2O, N_2, NO, N_2O, and NH_3. Figures 4 and 5 show that the calculated concentrations of NH_3, N_2O, NO and HNO_3 match closely with the available data [42]. The N_2 species concentration, however, is slightly over-predicted. It should be noted that NO_2 and HONO could not be separated in mass-spectra experiments due to their

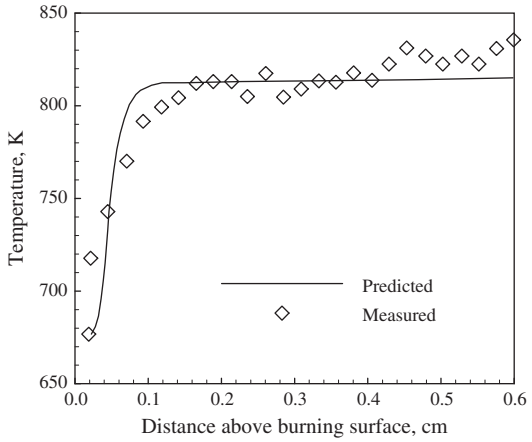

Fig. 3. Predicted and measured profiles of temperature at 3 atm.

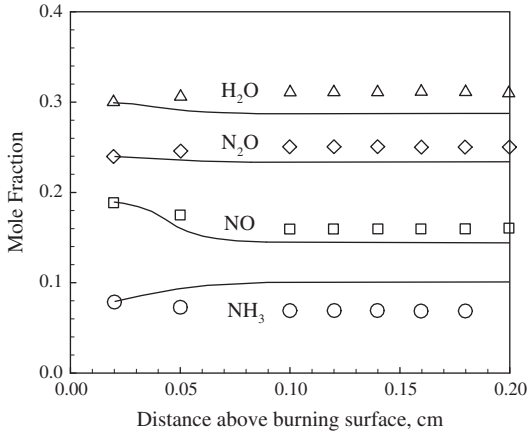

Fig. 4. Predicted and measured profiles of species mole fractions at 3 atm.

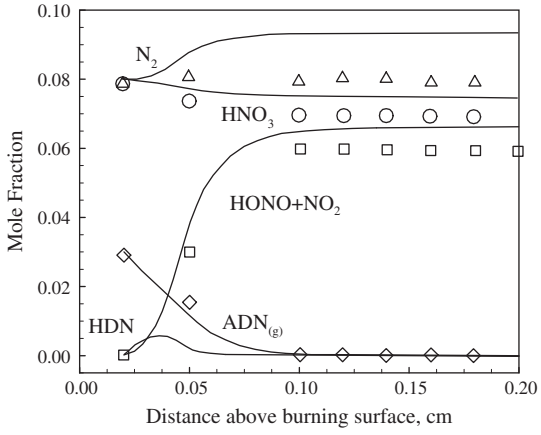

Fig. 5. Predicted and measured profiles of species mole fractions at 3 atm.

Table 5
Boundary conditions for gas phase flame calculation.

P (atm)	x[a] (mm)	$\dot{m}''$ (g/cm^2/s)	NH_3	H_2O	N_2	NO	N_2O	$ADN_{(v)}$	HNO_3	O_2	Ref.
3	0.2	2.15	0.08	0.30	0.08	0.19	0.24	0.03	0.08	–	[25]
6	4.19	3.4	0.0675	0.35	0.07	0.25	0.2225	–	0.04	–	[17]
40	1.5	3.85	–	0.42	0.18	0.21	0.14	–	–	0.05	[52]

[a] x is the distance above the propellant burning surface.

close molecular weights (46 g/mol for NO2, 47 g/mol for HONO). The prediction of combined NO_2 and HONO concentrations is quite close to the measurements.

Figure 5 shows that small concentration of $HN(NO_2)_2$ (i.e., HDN) is predicted close to the burning surface. The presence of HDN in the ADN gas flame was confirmed by Korobeinichev [25], although the mole fraction profile was not reported. It was considered to be an important species that decomposes (R4) in the near-surface region, prompting the partial oxidation of NH_3 (R6). In the same zone (0–0.1 cm), there is a temperature rise of about 150 K.

Figure 6 shows the entire ADN gas-phase flame structure at 3 atm. The four-zone flame structure showing the temperature rise to 820 K (0.1–4 cm), 1350 K (4–9 cm), 1680 K (10–25 cm), and finally to 2100 K (55–100 cm) is clearly seen. The latter three flames occur at far downstream locations and therefore can be practically observed only at high pressures. The major exothermicity in the second flame zone (~1350 K) is due to NH_3 oxidation reactions by NO_2 R6, R7, and R8. The corresponding heat-releasing mechanisms in the 3rd and 4th flames are the conversion of N_2O and NO to N_2, respectively. The existence of a region close to the propellant surface, where the temperature gradient is close to zero was obtained both in predicted and measured [24] temperature profiles (0–0.3 mm). A non-luminous region, also known as dark zone, is seen at ~0.1–2 cm, marked by a plateau in the temperature profile. In the pressure range of 5–40 atm, dark-zone temperature plateaus were observed experimentally from 843 to 1273 K [39]. The existence of such dark zones in nitrate esters and nitramine propellants has been addressed in detail by Yang et al. [53]. Figures 7 and 8 show a comparison of predicted and measured profiles of temperature and species mole fractions of ADN gas flame at 6 atm. The agreements are very good.

The present calculation results were compared with those of Liau et al. [17] and Korobeinichev et al. [25]. The boundary conditions used are identical, and the only difference is in the gas-phase kinetics mechanisms. Figures 9–12 show that the match obtained with experimental data using the current gas-phase kinetics mechanism is much better than the previous results from Liau et al. [17] and Korobeinichev et al. [25]. Subscripts "(0), (1), and (2)" indicate results from the present work, Liau et al. [17], and Korobeinichev et al. [25], respectively. The improvement in predictions derived by employing the optimal 34 species and 165 reactions gas-phase kinetics mechanism at 6 atm is evident.

Three distinct flames, which increase the gas-phase temperature to 1400 K (1–4 cm), 1840 K (5–15 cm), and 2100 K (25–100 cm) respectively, are shown in Fig. 13. The near-surface zone is not shown in the flame structure at 6 atm, since the model calculations began at 0.419 cm from the propellant surface, where the experimental boundary conditions for species were available as summarized in Table 5. Comparing the temperature and species profiles in Figs 6 and 13, it can be concluded that similar

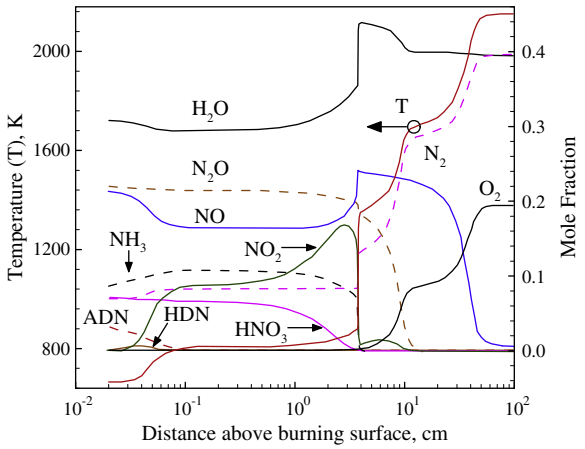

Fig. 6. Predicted temperature and species mole fractions at 3 atm.

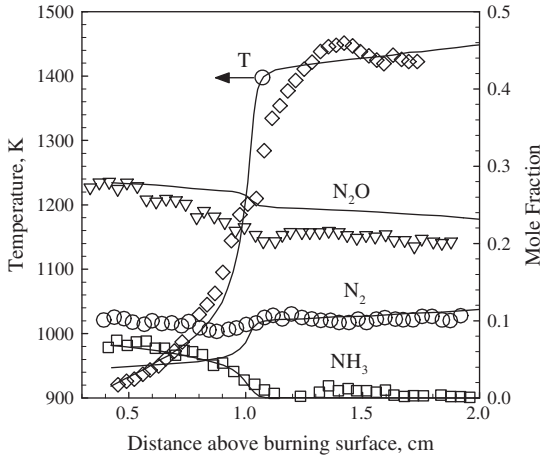

Fig. 7. Predicted and measured profiles of temperature and species mole fractions at 6 atm.

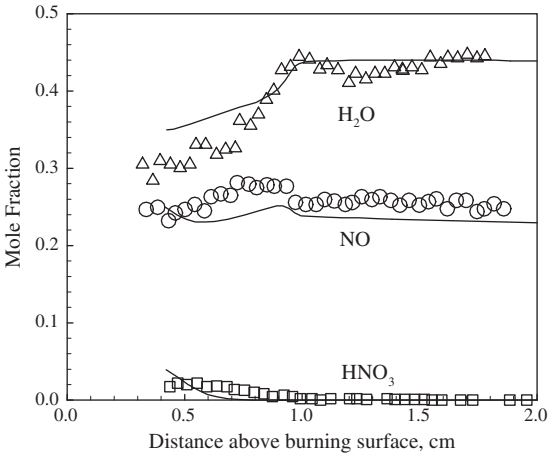

Fig. 8. Predicted and measured profiles of species mole fractions at 6 atm.

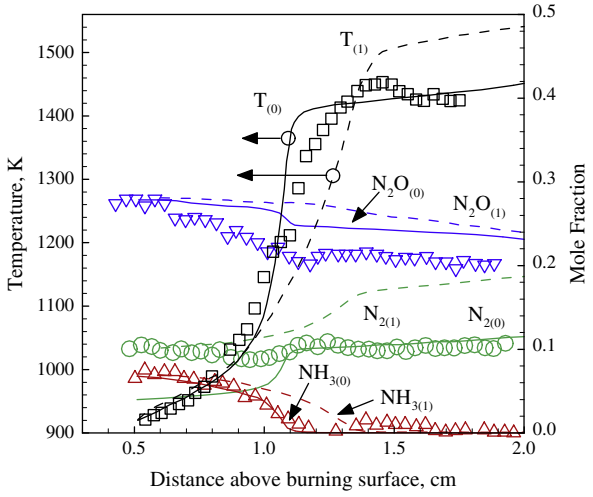

Fig. 9. Comparison of results of Liau et al. [17] and present study at 6 atm.

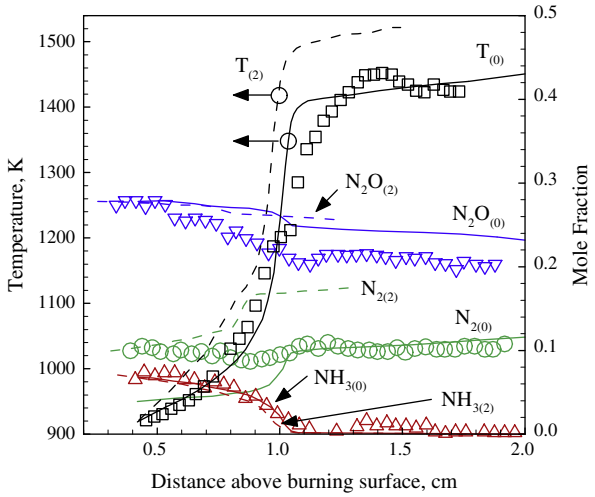

Fig. 10. Comparison of results of Korobeinichev et al. [25] and present study at 6 atm.

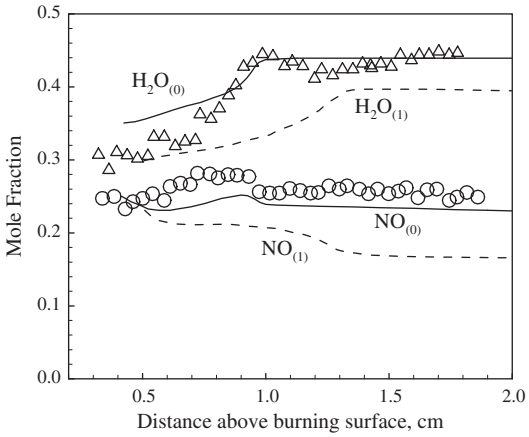

Fig. 11. Comparison of results of Liau et al. [17] and present study at 6 atm.

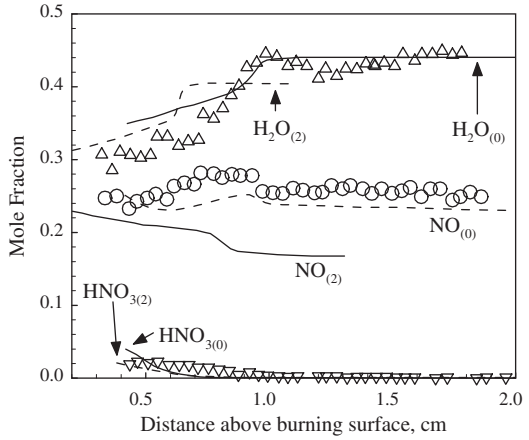

Fig. 12. Comparison of results of Korobeinichev et al. [25] and present study at 6 atm.

heat-release mechanisms are at play. There is a difference, however, in the location of the flames at the two pressures. The flames at 6 atm are closer to the propellant burning surface than their counterparts at 3 atm. Increase in pressure leads to a decrease in

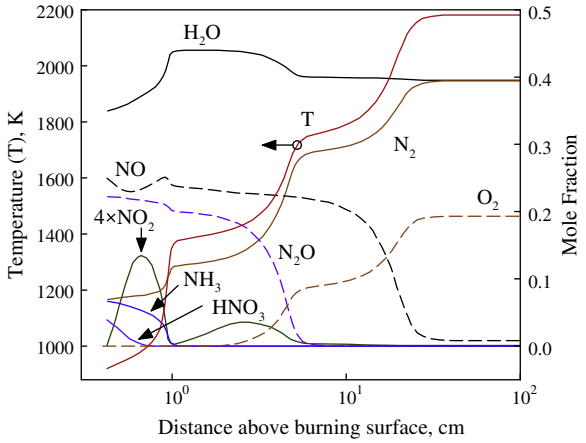

Fig. 13. Predicted temperature and species mole fractions at 6 atm.

the flame stand-off distance, due to the increase in the pressure-dependent reaction rates.

Figures 14 and 15 show a comparison of predicted (lines) and measured (symbols) profiles of temperature and species mole fractions of ADN gas-phase flame at 40 atm. The agreement again is quite good at high pressure. These calculations were started at 0.15 cm, due to the availability of species boundary conditions at that location, as described in Table 5. Figure 16 shows the entire flame structure of ADN in the gas phase. Only two distinct flames are seen here. The heat-release contribution of near-surface NH_3 oxidation reactions is not shown because the modeling domain extended from 0.15 to 10 cm. The conversion of N_2O and NO to N_2 is still the main source in second and third flames, respectively. The final flame occurs at ~10 cm, much closer than the corresponding ones observed at lower pressures.

Further analysis was performed to accurately estimate the affect of pressure on the flame structure and on the concentrations of some key species. Figures 17 and 18, respectively, show the near-surface view and the overall flame structure comparisons at 3, 6 and 40 atm. The flame stand-off distance is shortened sharply by increasing the pressure, due to enhanced reaction rates at elevated pressure. The agreement between measured and calculated temperature profiles at all the studied pressures is quite reasonable. The existence of dark-zone temperature plateaus at different

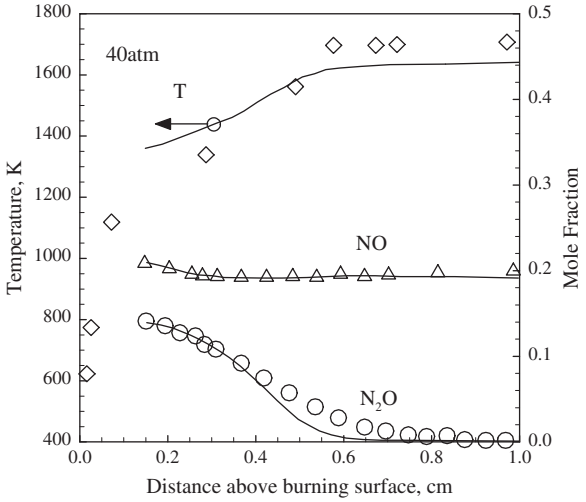

Fig. 14. Predicted and measured profiles of temperature and mole fractions at 40 atm.

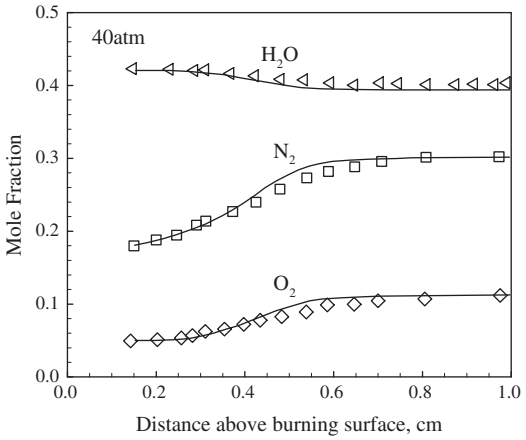

Fig. 15. Predicted and measured profiles of species mole fractions at 40 atm.

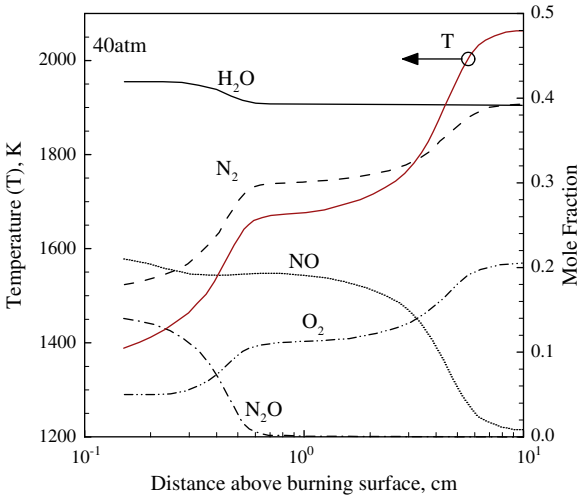

Fig. 16. Predicted profiles of temperature and species mole fractions at 40 atm.

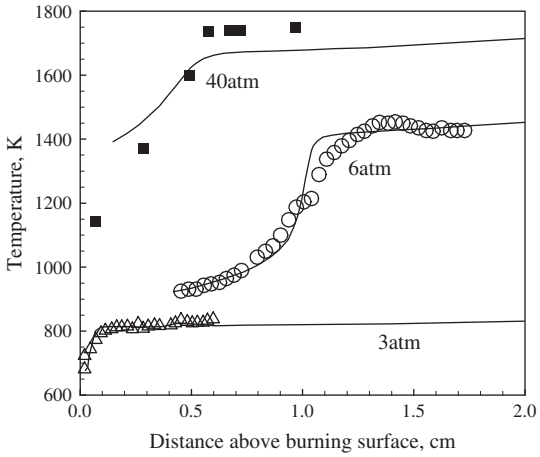

Fig. 17. Calculated and measured temperature profiles at various pressures (0–2 cm).

pressures close to the burning surface is also predicted well. Figures 19 and 20 show the influence of pressure on major species (H_2O, N_2, O_2, and NO). The contours of species mole fraction profiles look similar in shape, except that the pressure increase has displaced the curves closer to the burning surface. The final products H_2O, N_2, O_2, and NO and their mole fractions (0.396, 0.395, 0.194, and 0.008, respectively), at various pressures (shown in Figs. 6, 13 and 16) are quite close. Pressure has little influence on ADN final combustion products. It should also be noted that the mole fraction of NOx in final products is less than 1%, making ADN an environmentally friendly propellant.

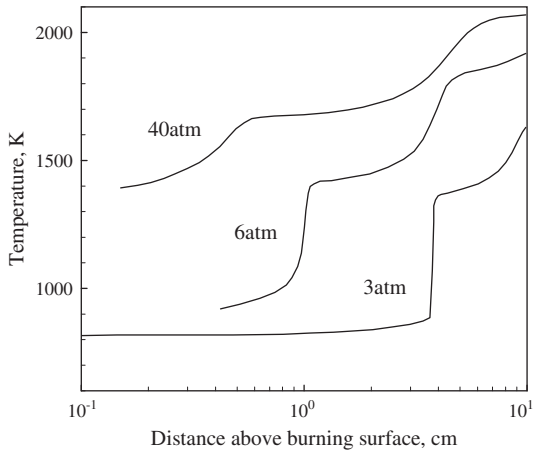

Fig. 18. Temperature profiles at various pressures (0.1–10 cm).

The modeling results show that the current 34 species and 165 reactions ADN gas-phase kinetics mechanism can adequately predict the ADN combustion flame structures at low and medium pressures. The profiles of flame temperature and species mole fractions at pressures exceeding 40 atm have not yet been obtained/compared, due to the lack of experimental data for appropriate boundary conditions. The reliability of current the ADN gas-phase kinetics mechanism in predicting temperature and species mole fractions at pressures higher than 40 atm should be further evaluated.

4.2. Coupled gas and condensed phase analysis

The results calculated by the coupled condensed- and gas-phase combustion model are shown and discussed in this subsection. Figure 21a and b, respectively, show the comparison between predicted (line) and measured [25] (symbols) temperature profiles in ADN gas phase flame at 6 atm and 40 atm. The temperature profile is shown starting from the propellant burning surface. At 6 atm, the agreement between predictions and data is excellent up to 1.4 cm above the propellant surface. The difference in values

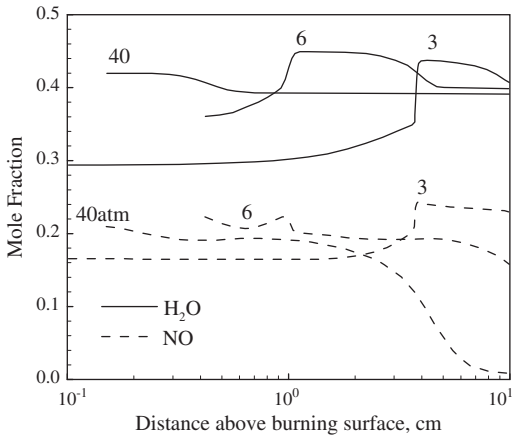

Fig. 19. Species mole fraction profiles at various pressures (0.1–10 cm).

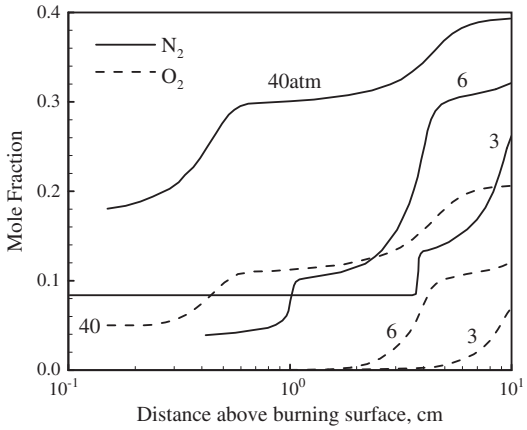

Fig. 20. Species mole fraction profiles at various pressures (0.1–10 cm).

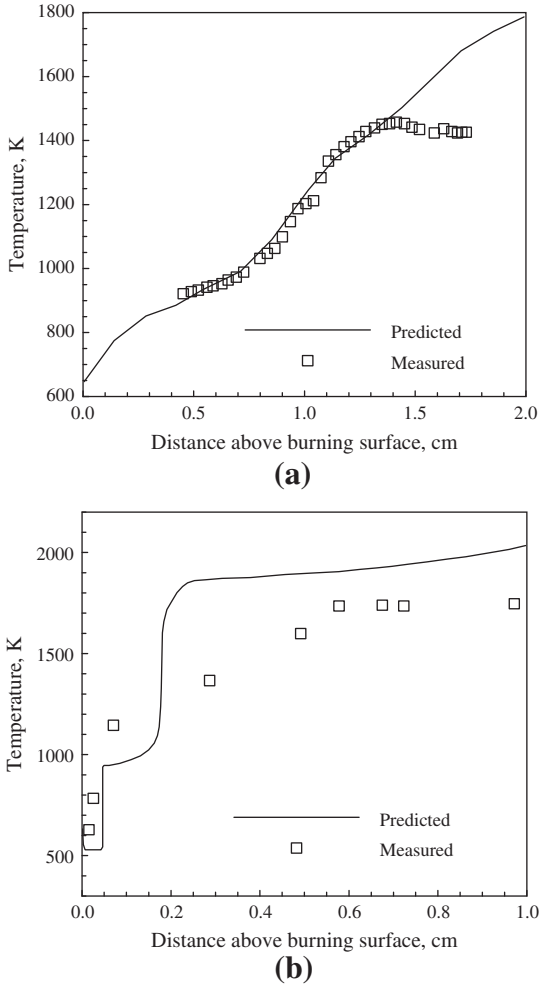

Fig. 21. (a) Predicted (line) and measured (symbols) temperature profile at 6 atm. (b) Predicted (line) and measured (symbols) temperature profile at 40 atm.

increases to about 12% at 1.8 cm. At 40 atm, the overall flame structure is also well captured. There appears to be a dark-zone formation before the final flame is established. The disagreement further away from the burning surface at both pressures is mainly due to some heat loss in the experiments, which was not accounted for in the current model. Secondly, the uncertainties in kinetics data of some global reactions in the condensed phase and intermediate reactions in the gas-phase may also lead to errors in predicted temperature profile closer to the surface.

Figure 22a and b, respectively, show the predicted (lines) and measured (symbols) mole fractions distribution of major species in ADN gas flame at 6 atm and 40 atm, by utilizing the coupled condensed- and gas-phase analysis. The agreements are reasonable. N_2O mole fraction is slightly over-predicted, while NO mole fraction is underpredicted closer to the surface (0–1 cm). The disagreement close to the burning surface could be attributed to the global ADN decomposition reaction (R10) and its kinetics, which was based on the available data for 1 atm. The disagreement in N_2 and N_2O away from the surface could be due to the heat loss in experiments which was not treated in the model. The development of more detailed semi-global ADN condensed kinetics may help improve predicted mole fraction profiles close to the propellant burning surface.

Figures 23 and 24 show detailed distributions of temperature and major species mole fractions at 6 atm in the foam layer underneath the propellant surface. The temperature increases monotonically in the foam layer from the ADN melting front to about 640 K near the surface. The decomposition of the condensed-phase ADN reaches about 80% within the foam layer and the void fraction, φ, is close to 0.95 at the burning surface. The ADN vapor mole fraction reaches a value of 0.15 at the surface, which is higher than the theoretical value of 0.05 suggested by Gross et al. [21]. The value of AN mole fraction at the propellant burning surface is around 0.04.

Figure 25 shows the temperature profiles underneath the propellant surface at three pressures ranging from 6 to 120 atm. The

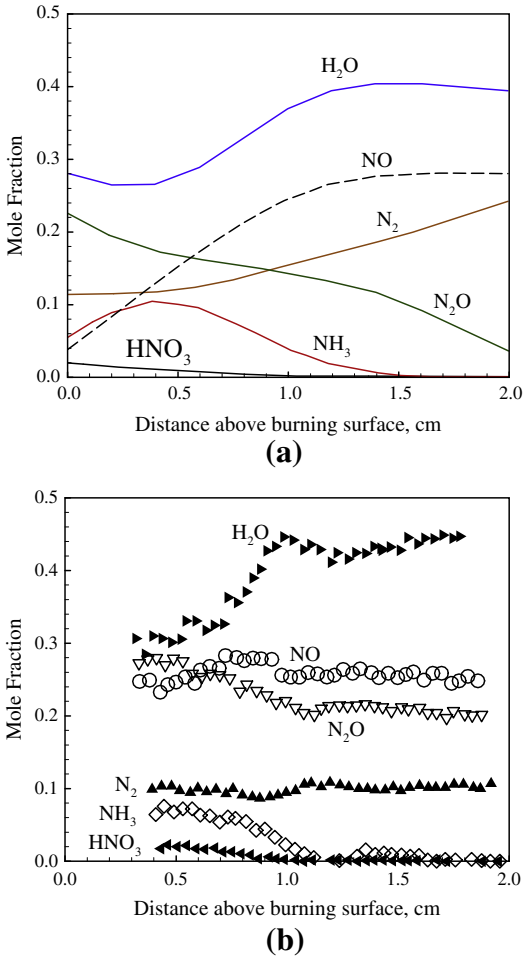

Fig. 22. Predicted (lines) and measured (symbols) mole fractions at 6 atm. (a) Species mole fraction profiles predicted by current model. (b) Species mole fraction distribution measured by Korobeinichev et al. [25].

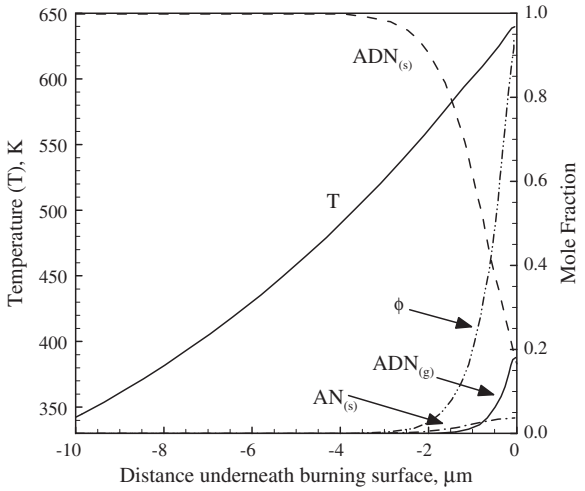

Fig. 23. Predicted temperature and species mole fractions profiles in foam layer at 6 atm.

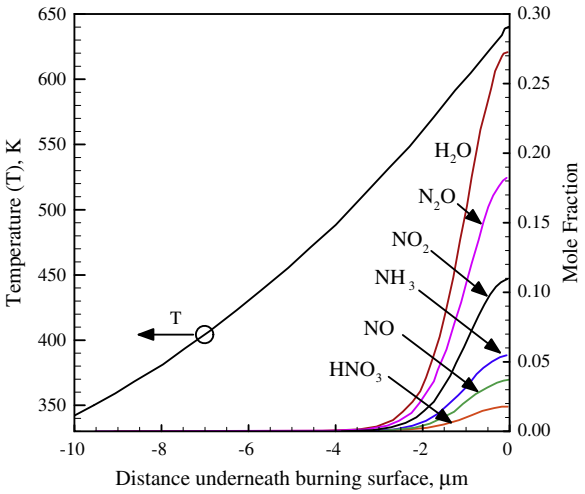

Fig. 24. Predicted species mole fractions profiles in foam layer at 6 atm.

thickness of the foam layer decreases with increasing pressure. Figure 26 shows the corresponding temperature profiles in the gas-phase region above the propellant surface. The final flame stand-off distance decreases drastically at higher pressures, resulting in a sharp temperature gradient increase at the propellant burning surface. At elevated pressure, a steeper gradient leads to a substantial increase of heat feedback from gas phase flame to foam layer. Consequently, the foam layer will decompose at a faster rate, thereby reducing its thickness.

Figures 27–29, respectively, compare the mole fractions of $ADN_{(s)}$, $ADN_{(g)}$, $AN_{(s)}$ at various pressures. While the $ADN_{(s)}$ mole fraction at the burning surface increases with the pressure, the $ADN_{(g)}$ and $AN_{(s)}$ mole fractions show the opposite trend. The decrease in the foam-layer thickness at higher pressures reduces residence time for the solid ADN to decompose. At lower pressures, solid ADN decomposes completely in the foam layer, while at elevated pressures only a part of ADN decomposes at the surface and the rest evaporates/pyrolyzes at the propellant burning surface. This indicates that the dominant pathways of solid ADN decomposition at lower pressure are condensed-phase reactions (R10) and (R11). The major pathways of solid ADN decomposition at elevated pressures, however, could be a combination of R10, R11, and R12.

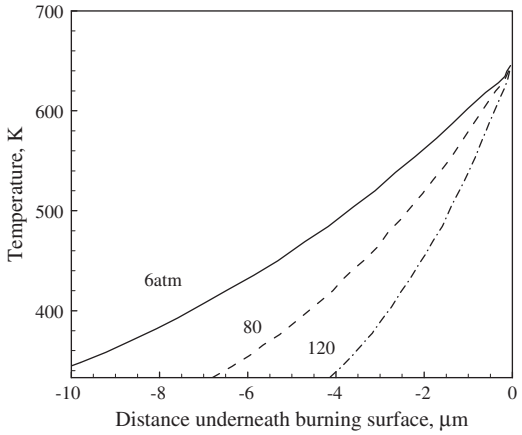

Fig. 25. Effect of pressure on temperature profiles underneath the burning surface.

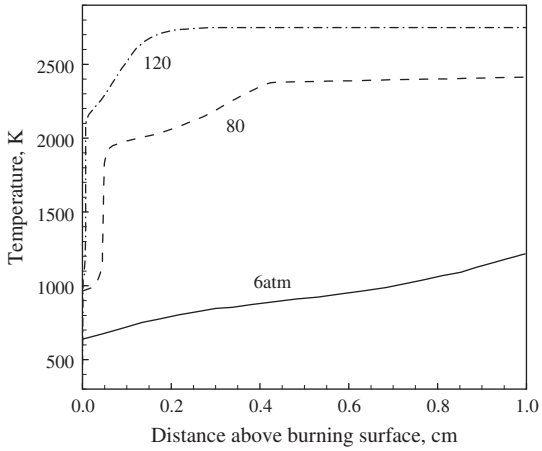

Fig. 26. Effect of pressure on temperature profiles in gas phase.

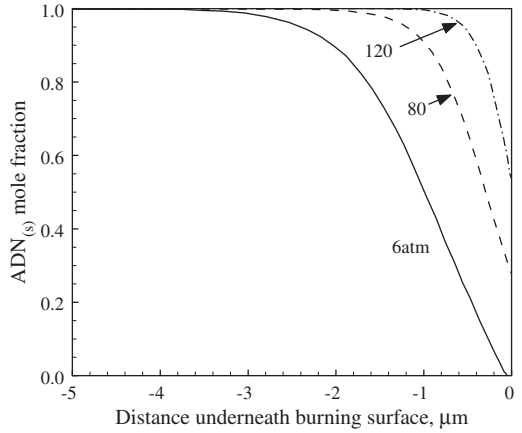

Fig. 27. Effect of pressure on $ADN_{(s)}$ mole fraction profiles underneath burning surface.

Further, it is clear that since less solid ADN decomposes at higher pressures, the mole fraction of solid AN at the propellant surface is smaller, as shown in Fig. 29. Figure 30 indicates that the void fraction at the burning surface decreases with increase in pressure. The values are 0.95 and 0.16 at 6 and 120 atm, respectively, indicating less $ADN_{(g)}$ and fewer gas bubbles in the foam layer at

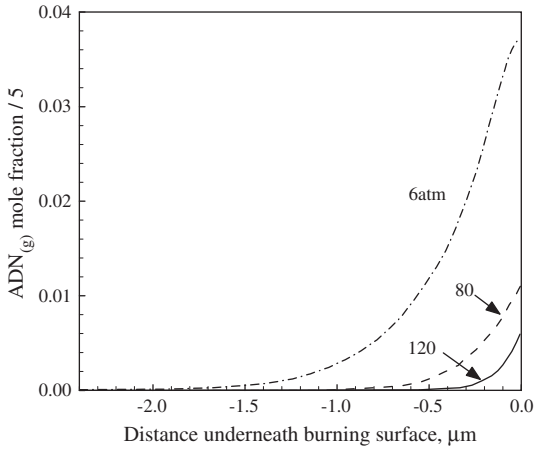

Fig. 28. Effect of pressure on $ADN_{(g)}$ mole fraction profiles underneath burning surface.

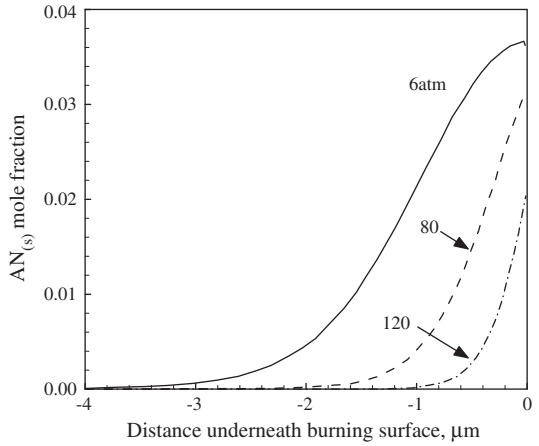

Fig. 29. Effect of pressure on $AN_{(s)}$ mole fraction profiles underneath burning surface.

elevated pressures. The void fraction trend agrees with that of the solid ADN mole fraction.

In the previous section, only gas-phase combustion was modeled, and the experimental burning rates shown in Table 5 were used as input conditions at different pressures. With the coupled condensed- and gas-phase combustion model, however, the burning rate can be predicted as a part of the solution. Figure 31 shows the calculated and experimentally measured burning rates at various pressures up to 350 atm, using the combined condensed- and gas-phase kinetics. A very good agreement is achieved in the pressure ranges of 0.7–40 atm and 100–350 atm.

There seems to be appreciable scatter in all the available experimental data in the pressure range of 20–100 atm. Around this range, ADN exhibits atypical burning behavior; the burning rate actually decreases with the increase in pressure, as evident in Fig. 31. This observation has been confirmed recently through the measurements conducted by Sinditskii et al. [23]. The calculated burning rates from the current model in this pressure range mimic the overall downward trend, although the predicted burning rates are lower. The current model seems to be able to capture the physiochemical phenomenon that is responsible for the irregular burning behavior of ADN propellant in the mid-pressure range. Table 6 shows the derived rate coefficients and corresponding pressure exponents for fitting the Saint Robert's law for the three different pressure ranges. The negative pressure exponent for the range of 60–100 atm shows the irregularity in the burning rate of ADN in this range.

The combined condensed- and gas-phase analysis also enables us to predict the propellant burning surface temperature as a part of the solution. Figure 32 shows the propellant surface temperature as a function of pressure. Considering that there is a substantial data scatter in the different experimental measurements, the calculated values are reasonable. It should be noted that it is difficult to precisely locate the propellant surface during combustion, due to the presence of foam layer and the ensuing bubbles; this makes it difficult to measure the surface temperature. In general, the surface temperature is expected to increase with the pressure, as captured by the current model. But looking closely at the pressure range of the irregular burning, it can be seen that the surface temperature actually drops, before starting to rise again at very high pressures.

4.3. ADN combustion irregularity

The changes in the flame structure, burning-surface rheology, and subsurface morphological structure exert a significant influence on the ADN burning characteristics. ADN combustion is stable at low and high pressures, but becomes irregular in the range of 20–100 atm, as shown in Fig. 31. The coupled condensed- and gas-phase analysis used in the current model provides some insight into the physiochemical phenomena that could explain such

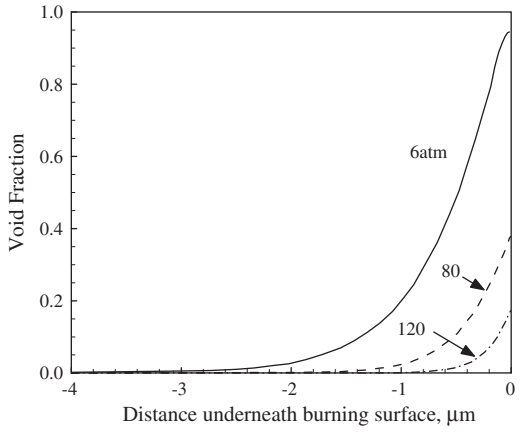

Fig. 30. Effect of pressure on void fraction profiles underneath burning surface.

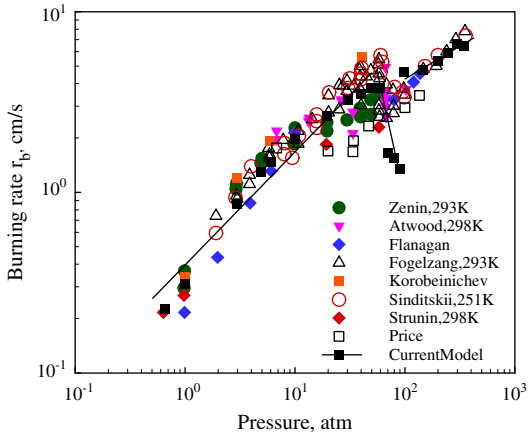

Fig. 31. Calculated and measured ADN propellant burning rates at various pressures.

Table 6
Predicted burning-rate law of pure ADN.

Pressure interval (MPa)	$r_b = ap^n$	
	a	n
0.2–6.08	16.8	0.54
6.08–9.12	75.9	−0.774
10.13–35.46	21.11	0.316

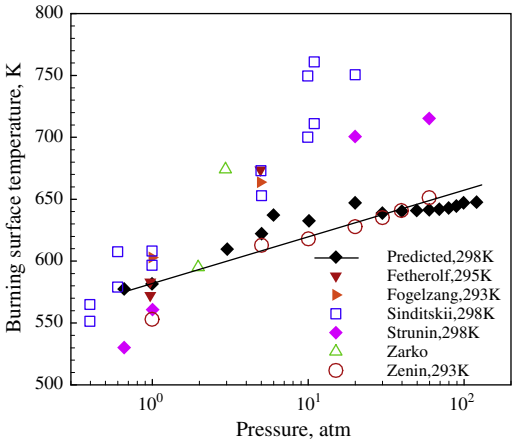

Fig. 32. ADN propellant burning surface temperature at various pressures.

a behavior. At lower pressures, decomposition of dinitramide in the condensed phase is maintained by the heat release during the formation of AN and N_2O [30]. It is clear from Figs. 29 and 30, respectively, that AN concentration and void fraction are higher at lower pressures. The exothermic condensed-phase processes dictate the burning rate at low pressure, since the heat feedback (gradient of the temperature profile at the propellant surface in Fig. 26) from the gas phase to the propellant accounts for only a small fraction of energy required to pyrolyze ADN.

At pressures greater than 100 atm, the foam layer is very thin and there is not much heat-release contribution from the condensed-phase. The secondary gas flame merges into the primary flame as shown in Fig. 26. Such rapid enhancement of the heat release near the propellant surface and its ensuing heat feedback to the condensed phase is sufficient for ADN pyrolysis. Hence, at pressure above 100 atm, the gas-phase heat release dictates the propellant burning behavior. In the mid-pressure range (20–100 atm), however, the condensed-phase heat release is low because the foam layer is relatively thinner. The final gas-phase flame still sits relatively farther from the propellant surface, resulting in lower heat feedback, as compared to the pressures greater than 100 atm. The burning irregularity may result from a competitive influence of the condensed-phase and gas-phase exothermic reactions in determining the propellant surface conditions and the associated burning rates. In this mid-pressure range, a gap between the energy required to pyrolyze ADN and the condensed-phase heat release causes the burning rate to decrease. Thus, the current model is able to capture the irregular combustion of ADN, and the results corroborate the explanation provided in Refs. [24,30].

4.4. Parametric analysis

Because several different sources are available in the literature for some of the ADN properties, there is a need to do parametric analysis to identify the most appropriate values to be used in the current model. Some of these uncertainties are reflected in the overall predictions made by the model. In particular, the thermodynamics and transport properties of solid and liquid ADN have some uncertainty. Table 1 shows the property values that were available from different sources. A series of numerical experiments were performed to identify values that yielded a closest match with the experimental data for temperature and species mole fraction profiles. The values that were finally chosen for use in the model appear in bold in Table 1. It should also be noted that some of properties were only mentioned for a specific temperature range. For example, $c_{p,\mathrm{ADN}(s)} = 2.094 \times 10^{-1} + 3.361 \times 10^{-4}$ and $\lambda_{p,\mathrm{ADN}(s)} = 1.238 \times 10^{-3} - 5.78 \times 10^{-7}\,T$ are only valid from 293 to 338 K, although validity was assumed in a much wider temperature range, from 293 to 650 K.

Table 7
Kinetic data for ADN global decomposition reaction (R10).

A	Ea (kcal/mol)	Ref.
1.67e7	11.5	[25]
3.5e15	**32.0**	
9.9e11	29.6	[33]
5.5e13	32.8	
1.4e15	36–40	
8.8e16	36–40	
1.4e15	36–40	
8.8e16	36–40	
4.0e15	38.0	
1.0e21	47.8	[13]
2.5e14	35.5	[7]
1.0e20	30–41.8	[26]
1.46e16	38.5	[22]
1.3e15	35.5	

Other than the thermodynamic and transport properties, the kinetics data associated with the global reactions (R10) and (R12) have some uncertainty, due to the range of values available in the literature. The global reaction (R11), on the other hand, has been extensively studied and the broadly acceptable kinetics parameters [50] have been employed without the need of any parametric study. Table 7 lists the kinetics data available for R10, along with the corresponding references. Based on the detailed parametric study, the value that yielded the closest match with experimental data appears in bold. For thermodynamic phase transition (R12) of ADN, among the several sets of vapor pressure correlations, the one used by Gross et al. [21] was found to give the best results.

There are several reasons for the deviation of the predictions from the experimental measurements, including the use of 1-D adiabatic approach, uncertainties in condensed-phase ADN properties and their global kinetics, and uncertainties in the kinetics of some gas-phase reactions close to the burning surface. The use of 1-D approach neglects the inherent 2-D nature of gas-phase flame expansion. The adiabatic treatment neglects heat losses occurring away from the burning surface and tends to over predict the final flame temperature. The condensed-phase global kinetics needs a more detailed or semi-global kinetics approach, but the lack of experimental data limits the modeling improvement. Although the detailed gas-phase mechanism yields satisfactory predictions, it is important to note that kinetics scheme is usually established for low pressures. Extrapolation of these results to high-pressure conditions requires caution and further consideration.

5. Conclusions

A comprehensive numerical analysis has been conducted to study the key physiochemical processes involved in ADN propellant combustion. The theoretical formation is based on a multi-phase treatment, wherein conservation equations of mass, energy, and species concentrations for condensed and gas phases are solved. The model takes into account the finite-rate chemical

kinetics in both phases. While three global reactions are considered in the condensed phase, an optimized 34-species and 165-reactions detailed kinetics scheme is employed for resolving the gas-phase chemistry. The model has been applied to predict the detailed flame structure of ADN over a broad range of pressures. Parametric studies were performed to pick the thermodynamic and transport properties of the condensed phase from the data available in the literature. Temperature and species mole fraction profiles, burning rates, and surface temperatures were studied to fully characterize the ADN combustion-wave structure in both the condensed and gas phases. Reasonably good agreements between predicted and measured profiles of temperature and species were obtained by employing the current gas-phase kinetics. Results show noticeable improvement in the predictions as compared to the previous studies. The final combustion products are chlorine free and the mole fraction of the pollutant NO_x is less than 1% at all pressures, showing that ADN is an environmentally friendly propellant.

Using the coupled condensed and gas-phase combustion model, the predicted and measured burning rates were found to match closely over a broad range of pressures (0.7–350 atm). The burning rate increases with pressure, except in the range of 40–100 atm. The model was able to capture the irregular burning behavior in this mid-pressure range. At lower pressures below 20 atm, ADN combustion is characterized by intense energy release in the condensed phase, weak heat feedback from the gas phase, and high burning rate. Above 100 atm, the secondary flame merges with the primary flame, causing rapid enhancement in the heat feedback to the propellant surface. The intense gas-phase heat feedback dictates the burning surface condition. In the mid-pressure range, however, the combustion irregularity may be attributed to the competitive influence of the condensed-phase and gas-phase exothermic reactions in determining the propellant surface conditions and the associated burning rates. In this range, the gap between the energy required to pyrolyze ADN and the condensed-phase heat release causes the burning rate to decrease.

There are some limitations and uncertainties in the present ADN combustion model, which cause some deviation between the predictions and experimental data. The uncertainty in condensed-phase ADN global reactions and their kinetics is one of the major limitations. Gas-phase reactions close to the burning surface should also be further studied. For better predictions of final flame temperatures at low pressures, the heat loss that occurs away from the burning surface must be accounted for. The current combined condensed- and gas-phase kinetics model for ADN combustion is promising, but needs further development. A semi-global or even detailed chemical reaction approach in the condensed phase would greatly improve the model predictions. More accurate thermodynamic and transport properties for solid and liquid ADN and its thermal decomposition products would also be very helpful.

Acknowledgments

The authors gratefully acknowledge support from the John L. and Genevieve H. McCain Endowment of the Pennsylvania State University and the William R.T. Oakes Endowment of the Georgia Institute of Technology. This work was initiated in 2007 when the authors were affiliated with the Pennsylvania State University.

References

[1] O.P. Korobeinichev, in: V. Yang, T.B. Brill, W.Z. Ren (Eds.), Solid Propellant Chemistry, Combustion, and Motor Interior Ballistics, Progress in Astronautics and Aeronautics, vol. 185, AIAA, Reston, VA, 2000. pp. 335–350.
[2] O.A. Luk'yanov, V.P. Gorelik, V.A. Tartakovsky, Russ. Chem. Bull. 43 (1994) 89–92.
[3] O.A. Luk'yanov, V.A. Tartakovsky, in: V. Yang, T.B. Brill, W.Z. Ren (Eds.), Solid Propellant Chemistry, Combustion, and Motor Interior Ballistics, Progress in Astronautics and Aeronautics, vol. 185, AIAA, Reston, VA, 2000. pp. 207–220.
[4] M.B. Talawar, R. Sivabalan, M. Anniyappan, G.M. Gore, S.N. Asthana, B.R. Gandhe, Combust. Explos. Shock Waves 43 (2007) 62–72.
[5] R.J. Schmitt, J.C. Bottaro, D.S. Ross, P.E. Penwell, Dinitramide Salts and Method of Making Same, US Patent 5254324.
[6] R.J. Schmitt, Bottaro, P.E. Penwell, Method of Forming Dinitramide Salts, US Patent 5198204.
[7] V.A. Strunin, A.P. D'Yakov, G.B. Manelis, Combust. Flame 117 (1999) 429–434.
[8] M.J. Rossi, J.C. Bottaro, D.F. McMillen, Int. J. Chem. Kinet. 25 (1993) 549–570.
[9] A.A. Zenin, V.M. Puchkov, S.V. Finjakov, AIAA Paper 99-0595, 1999.
[10] A.I. Atwood, T.L. Boggs, P.O. Curran, T.P. Parr, D.M. Hanson-Parr, C.F. Price, J. Wiknich, J. Propul. Power 15 (1999) 740–747.
[11] A.I. Atwood, T.L. Boggs, P.O. Curran, T.P. Parr, D.M. Hanson-Parr, J. Propul. Power 15 (1999) 748–752.
[12] O.P. Korobeinichev, A.A. Paletsky, Combust. Flame 127 (2001) 2059–2065.
[13] C.A. Wight, S. Vyazovkin, in: 33rd JANNAF Combustion Meeting, CPIA Publication No. 653, vol. II, 1996, pp. 127–133.
[14] A.M. Mebel, M.C. Lin, C.F. Melius, K. Morokuma, J. Phys. Chem. 99 (1995) 6842–6848.
[15] P. Politzer, J.M. Seminario, M.C. Concha, J. Mol. Struct. (Theochem.) 427 (1998) 123–129.
[16] J. Park, D. Chakraborty, M.C. Lin, in: 27th Symposium (International) on Combustion, The Combustion Institute, 1998, pp. 2351–2357.
[17] Y.-C. Liau, V. Yang, M.C. Lin, J. Park, in: 35th JANNAF Combustion Meeting, CPIA Publication No. 685, vol. II, 1998, pp. 13–30.
[18] Y.-C. Liau, V. Yang, in: 36th JANNAF Combustion Meeting, CPIA Publication No. 691, vol. I, 1999, pp. 369–377.
[19] N.E. Ermolin, Interim (Annual) Report on the Study of the Chemical Structure of ADN Flame, 1996.
[20] N.E. Ermolin, Combust. Explos. Shock Waves 40 (2004) 92–109.
[21] M.L. Gross, M.W. Beckstead, K.V. Puduppakkam, M.G. Hawkins, AIAA Paper 2006-4747, 2006.
[22] T.B. Brill, P.J. Brush, D.G. Patil, Combust. Flame 92 (1993) 178–186.
[23] V.P. Sinditskii, V.Y. Egorshev, A.I. Levshenkov, V.V. Serushkin, J. Propul. Power 22 (2006) 769–776.
[24] V.P. Sinditskii, V.Y. Egorshev, A.I. Levshenkov, V.V. Serushkin, J. Propul. Power 22 (2006) 777–785.
[25] O.P. Korobeinichev, L.V. Kuibida, A.A. Paletsky, A.G. Shmakov, AIAA 98-0445, 1998.
[26] S. Vyazovkin, C.A. Wight, J. Phys. Chem. A 101 (1997) 5653–5658.
[27] T.P. Russell, G.J. Piermarini, S. Block, P.J. Miller, J. Phys. Chem. 100 (1996) 3248–3251.
[28] B.L. Fetherolf, T.A. Litzinger, Combust. Flame 114 (1998) 515–530.
[29] B.L. Fetherolf, T.A. Litzinger, in: 29th JANNAF Combustion Meeting, CPIA Publication No. 593, vol. II, 1992, pp. 327–338.
[30] R. Yang, P. Thakre, V. Yang, Combust. Explos. Shock Waves 41 (2005) 657–679.
[31] J.-K. Yoon, P. Thakre, V. Yang, Combust. Flame 145 (2006) 300–315.
[32] M.W. Beckstead, in: V. Yang, T.B. Brill, W.Z. Ren (Eds.), Solid Propellant Chemistry, Combustion, and Motor Interior Ballistics, Progress in Astronautics and Aeronautics, vol. 185, AIAA, Reston, VA, 2000. pp. 267–283.
[33] M.L. Gross, Two-Dimensional Modeling of AP/HTPB Utilizing a Vorticity Formation and One-Dimensional Modeling of AP and ADN, Ph.D. Dissertation, The Brigham Young University, Provo, UT, 2007.
[34] M.W. Beckstead, K.V. Puduppakkam, P. Thakre, V. Yang, Prog. Energy Combust. Sci. 33 (2007) 497–551.
[35] Y.-C. Liau, V. Yang, J. Propul. Power 11 (1995) 729–739.
[36] E.S. Kim, V. Yang, Y.-C. Liau, Combust. Flame 131 (2002) 227–245.
[37] A.A. Zenin, J. Propul. Power 11 (1995) 752–758.
[38] A.E. Fogelzang, V.V. Serushkin, V.P. Sinditskii, V.Y. Egorshev, Y.K. Shchipin, V.A. Tropynin, AIAA 98-0451, 1998.
[39] A.E. Fogelzang, V.P. Sinditskii, V. Yu Egorshev, in: Proc. of 28th Int. Annual Conf. of ICT, Karlsruhe, FRG, 1997, p. 99.
[40] L.K. Gusachenko, V.E. Zarko, Combust. Explos. Shock Waves 41 (2005) 20–34.
[41] R.A. Yetter, F.L. Dryer, M.T. Allen, J.L. Gatto, J. Propul. Power 11 (1995) 683–697.
[42] O.P. Korobeinichev, T.A. Bolshova, A.A. Paletsky, Combust. Flame 126 (2001) 1516–1523.
[43] A.G. Shmakov, O.P. Korobeinichev, T.A. Bol'shova, Combust. Explos. Shock Waves 38 (2002) 284–294.
[44] D.M. Hanson-Parr, T.P. Parr, J. Energy Mater. 17 (1999) 1–48.
[45] V.P. Sinditskii, V. Yu Egorshev, V.V. Serushkin, A.I. Levshenkov, in: Rocket Propulsion: Present and Future, Abstracts of the 8th Int. Workshop on Combustion and Propulsion, Pozzuoli, Naples, Italy, 2000, pp. 16–20.
[46] O.P. Korobeinichev, A.A. Paletsky, A.G. Tereschenko, E.N. Volkov, Proc. Combust. Inst. 29 (2002) 2955–2961.
[47] A.E. Scheidegger, The Physics of Flow through Porous Media, 3rd ed., Univ. of Toronto Press, Buffalo, NY, 1974.
[48] S.C. Li, F.A. Williams, S.B. Margolis, Combust. Flame 80 (1990) 329–349.
[49] G.F. Velardez, S. Alavi, D.L. Thompson, J. Chem. Phys. 119 (2003) 6698–6708.

[50] V.P. Sinditskii, V.Yu. Egorshev, V.V. Serushkin, A.I. Levshenkov, M.V. Berezin, S.A. Filatov, S.P. Smirnov, Thermochim. Acta 496 (1–2) (2009) 1–12.
[51] R.J. Kee, J.F. Grcar, M.D. Smooke, J. Miller, A Fortran Program for Modeling Steady Laminar One-Dimensional Premixed Flames, Sandia National Lab. Rep. SAND85-8240, December 1985.
[52] O.P. Korobeinichev, A.A. Paletsky, A.G. Tereschenko, T.A. Bolshova, in: K.K. Kuo (Ed.), Combustion of Energetic Materials, 2002, pp. 486–491.
[53] R.-J. Yang, P. Thakre, Y.-C. Liau, V. Yang, Combust. Flame 145 (2006) 38–58.